

Distinguishing Dark Matter, Modified Gravity, and Modified Inertia with the Inner and Outer Parts of Galactic Rotation Curves

KYU-HYUN CHAE¹

¹*Department of Physics and Astronomy, Sejong University, 209 Neungdong-ro Gwangjin-gu, Seoul 05006, Republic of Korea*

ABSTRACT

The missing gravity in galaxies requires dark matter, or alternatively a modification of gravity or inertia. These theoretical possibilities of fundamental importance may be distinguished by the statistical relation between the observed centripetal acceleration of particles in orbital motion and the expected Newtonian acceleration from the observed distribution of baryons in galaxies. Here predictions of cold dark matter halos, modified gravity, and modified inertia are compared and tested by a statistical sample of galaxy rotation curves from the Spitzer Photometry and Accurate Rotation Curves (SPARC) database. Modified gravity under an estimated mean external field correctly predicts the observed statistical relation of accelerations from both the inner and outer parts of rotation curves. There is a 5.1σ difference between the inner and outer parts on an acceleration plane which would be inconsistent with current proposals of modified inertia. Removing galaxies with possible systematic concerns such as central bulges or special inclinations does not change this trend. Cold dark matter halos predict a systematically deviating relation from the observed one. All aspects of rotation curves are most naturally explained by modified gravity.

Keywords: :Dark matter (353); Modified Newtonian dynamics (1069); Disk galaxies (391)

1. INTRODUCTION

Cold (having a clumpy property on galaxy scales) dark matter (CDM) is a key ingredient of the standard Λ CDM cosmological model. CDM has been popular since the 1980s as it seemed to provide a plausible framework for modeling the large-scale structure of the universe and galaxy formation (e.g., [White & Rees 1978](#); [Peebles 1982](#); [Blumenthal et al. 1984](#)). Modern Λ CDM modeling uses hydrodynamic simulations (e.g., [Di Cintio et al. 2014a](#); [Tollet et al. 2016](#); [Lazar et al. 2020](#)) to predict the structure of the dark matter halo embedding, nurturing, and interacting with the galaxy. However, the Λ CDM model is faced with serious challenges ([Kroupa 2012](#); [Famaey & McGaugh 2012](#); [Bull et al. 2016](#); [Bullock & Boylan-Kolchin 2017](#); [Di Valentino et al. 2021](#); [Abdalla et al. 2022](#); [Banik & Zhao 2022](#); [Perivolaropoulos & Skara 2022](#); see also [Peebles 2022](#) for an illuminating viewpoint). The concept of DM is tied with the standard gravitational dynamics of Newton and Einstein. Standard theory is unique in that it obeys the strong equivalence principle (SEP) by which the internal dynamics of a galaxy falling freely in a constant external field from surrounding structures is unaffected by the external field. Alternative theories of gravitational dynamics that break the SEP can replace the need for DM, as was theorized in the framework called modified Newtonian dynamics (MOND; [Milgrom 1983a](#)).

MOND makes several salient predictions ([Milgrom 1983a,b](#)) about galactic kinematics including the baryonic Tully-Fisher relation, the radial acceleration relation (RAR), and the external field effect (EFE) which is a manifestation of the SEP's breakdown. All these predictions were confirmed or being tested favorably by current data (e.g., [McGaugh 2005](#); [McGaugh et al. 2016](#); [Chae et al. 2020, 2021, 2022](#)). Theoretically, MOND can be realized by modified gravity ([Bekenstein & Milgrom 1984](#); [Milgrom 2010](#)), i.e., modified Poisson equations, or by modified inertia ([Milgrom 1994, 1999, 2022](#)), i.e., a modification of Newton's laws of motion, at accelerations weaker than about 10^{-10} m s⁻².

A rotation curve (RC) covering a large dynamic range from the higher-acceleration inner rising part to the lower-acceleration far outskirts may have an interesting discriminating power in testing CDM, modified gravity, and modified inertia. The observed circular rotation speed V at radius R in the midplane of the disk in a rotationally supported galaxy implies a radial (i.e., centripetal) acceleration

$$g_{\text{obs}}(R) = \frac{V^2}{R}, \quad (1)$$

while the observed baryonic (i.e., stars and gas) mass distribution $\rho_{\text{bar}}(R, z)$ implies a Newtonian radial acceleration

$$g_{\text{bar}}(R) = \left. \frac{\partial \Phi_{\text{N}}(R, z)}{\partial R} \right|_{z=0}, \quad (2)$$

where $\Phi_{\text{N}}(R, z)$ is the Newtonian potential satisfying the Poisson equation

$$\nabla^2 \Phi_{\text{N}} = 4\pi G \rho_{\text{bar}}, \quad (3)$$

where G is Newton's gravitational constant. The empirical relation between g_{obs} and g_{bar} (the RAR) provides an interesting testbed for competing theories.

Here an empirical RAR for up to 3097 ($g_{\text{bar}}, g_{\text{obs}}$) data points from up to 152 rotationally supported galaxies selected from the Spitzer Photometry and Accurate Rotation Curves (SPARC) catalog (Lelli et al. 2016) is compared with theoretical predictions or Markov chain Monte Carlo (MCMC) modeling results for CDM and MOND. For the first time, dark matter, modified gravity, and modified inertia are simultaneously tested and distinguished by considering separately the inner and outer parts of galactic rotation curves. The paper is organized as follows. In § 2.1, the data used in this work are described with an emphasis on the inner and outer parts of RCs. In § 2.2, I describe the methods concisely. In § 3, I describe the main results of this work. In § 4, I discuss the main results and draw a conclusion. The details of the methods can be found in Appendix A. The properties of DM halos derived from halo modeling are described in Appendix B.

2. DATA AND METHODS

2.1. Data

The SPARC database (Lelli et al. 2016) provides RCs and mass distributions of stars and gas for 175 rotationally supported galaxies ranging from dwarf galaxies to giant spiral galaxies. Rotation velocities $V_{\text{obs}}(R)$ as a function of cylindrical radius R are reported for a measured inclination angle i_{obs} . Baryonic mass distributions in the stellar and gas disks are reported as Newtonian rotation velocities $V_{\text{disk}}(R)$ and $V_{\text{gas}}(R)$ via Poisson's equation. Similarly, the stellar mass distribution in a bulge is reported as $V_{\text{bulge}}(R)$. The SPARC reported values of $V_{\text{disk}}(R)$ and $V_{\text{bulge}}(R)$ are based on stellar mass-to-light ratios at a wavelength of $3.6\mu\text{m}$ of $\Upsilon_{\text{disk}} = 0.5\Upsilon_{\star}$ and $\Upsilon_{\text{bulge}} = 0.7\Upsilon_{\star}$, where Υ_{\star} is the solar value. The SPARC reported values of $V_{\text{gas}}(R)$ are for gas-to-HI (neutral hydrogen) mass ratio of 1.33. The Newtonian rotation velocity of a test particle due to all observed baryons is given as $V_{\text{bar}} = \sqrt{V_{\text{disk}}^2 + V_{\text{bulge}}^2 + V_{\text{gas}}^2}$.

RCs are classified by a quality flag Q . There are 163 galaxies with RCs of good ($Q = 1$) or acceptable ($Q = 2$) quality. However, a recent study (Chae et al. 2021) finds that the RC of one galaxy (UGC 06787) is problematic, so this galaxy is excluded. In this study, the RAR based on the SPARC reported $V_{\text{obs}}(R)$ will be used to test various modeling and simulation results. Hence, nearly face-on galaxies with $i_{\text{obs}} < 30^\circ$ are excluded as in McGaugh et al. (2016) and Chae et al. (2020) to minimize $1/\sin i_{\text{obs}}$ corrections in $V_{\text{obs}}(R)$.¹ Then, we are left with 152 galaxies. These galaxies provide 3097 independent values of $V_{\text{obs}}(R)$ and the same number of $V_{\text{bar}}(R)$. Previous studies (McGaugh et al. 2016; Chae et al. 2020) applied a tight signal-to-noise ratio (S/N) cut on individual rotation velocities of $V_{\text{obs}}(R)$: velocities with $S/N \leq 10$ were not used. Such a cut would have discarded 469 velocities from the total of 3097 velocities from the chosen 152 galaxies. In this study, this cut is not applied for two reasons. First, the median of residuals from the RAR in a bin will be calculated through a Monte Carlo method fully considering individual errors. Thus, data with larger errors are proportionately less weighted, so that an artificial hard cut is not needed. Second and more importantly, velocities with $S/N \leq 10$ are mostly from the inner rising part of the RCs. Because the inner rising part

¹ For a recent cautionary tale in this regard, see Banik et al. (2022).

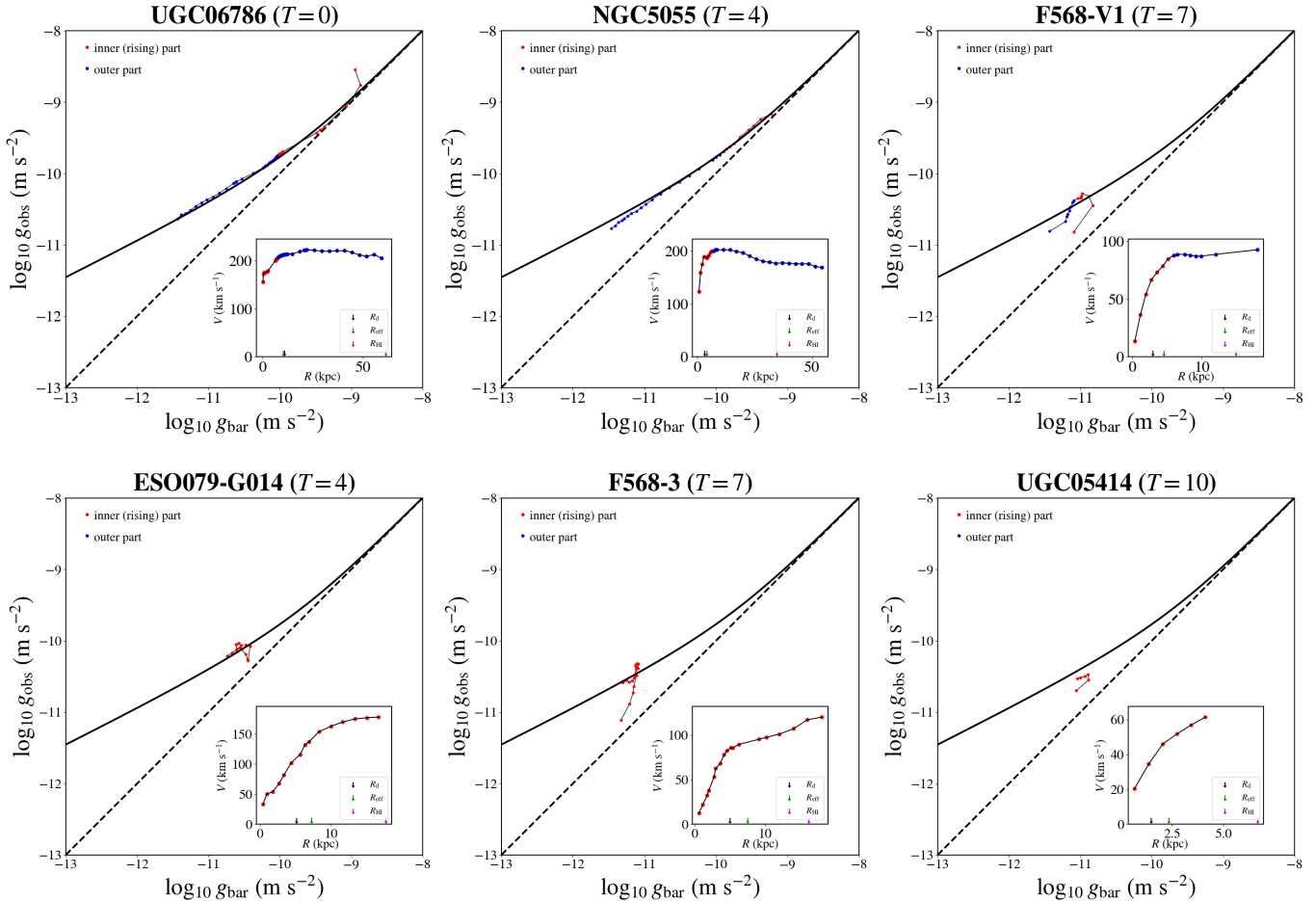


Figure 1. Examples of separating a rotation curve into the inner and outer parts. *Upper row:* Three rotation curves of different galaxy type T (as given in Lelli et al. 2016) are shown in the acceleration space based on AQUAL-fitted parameters (Chae et al. 2022). The inset shows the SPARC reported rotation curves. The inner rising and outer quasi-flat parts were separated visually. A clear inner-outer separation such as these can be done for about 70% of SPARC galaxies (see the text). *Lower row:* Examples in which the outer quasi-flat part is unobserved or ill-defined from the SPARC database. For the galaxies without the outer part, AQUAL-fitting (Chae et al. 2022) is not available and thus original SPARC mass models are shown here.

can be used to distinguish between modified gravity and modified inertia, it is better to keep all velocities of the inner part to maximize the statistical power.

The inner and outer parts of an RC are determined visually because observed RCs have various shapes. Examples of the separation of a rotation curve into the inner and outer parts can be found in the upper row of Figure 1. There are also extreme cases where the RC rises up to the last measured point as shown in the lower row of Figure 1, or no rising part is observed at all. A high-density bulge or a baryon-dominated extended gas disk can play a significant role. Thus, the transition point between the inner rising part and the outer quasi-flat part can vary greatly. For about 30% of galaxies the RC rises up to the last measured point (although it is not so clear-cut in some cases) so that the outer part is absent or ill-defined. In those cases, the outermost measured radius is simply taken as (the lower limit of) the transition radius R_{turn} and thus all data points belong to the inner part.² The transition radius ranges from ≈ 0 to $\approx 9R_d$ where R_d is the stellar disk scale radius (see Appendix A).

The distribution of visually determined transition radii for the selected 152 galaxies can be found in Figure 2. The median transition radius is $2.6R_d$. The ratio R_{turn}/R_d is anti-correlated with galaxy luminosity as shown in the lower panel of Figure 2. This is consistent with the empirical fact that giant spiral galaxies have an extended outer part

² While a lower limit can only be set on the transition radius in such cases, the membership of data points in the inner part is unchanged by the underestimated transition radius. As long as the membership is correct, this work is unaffected.

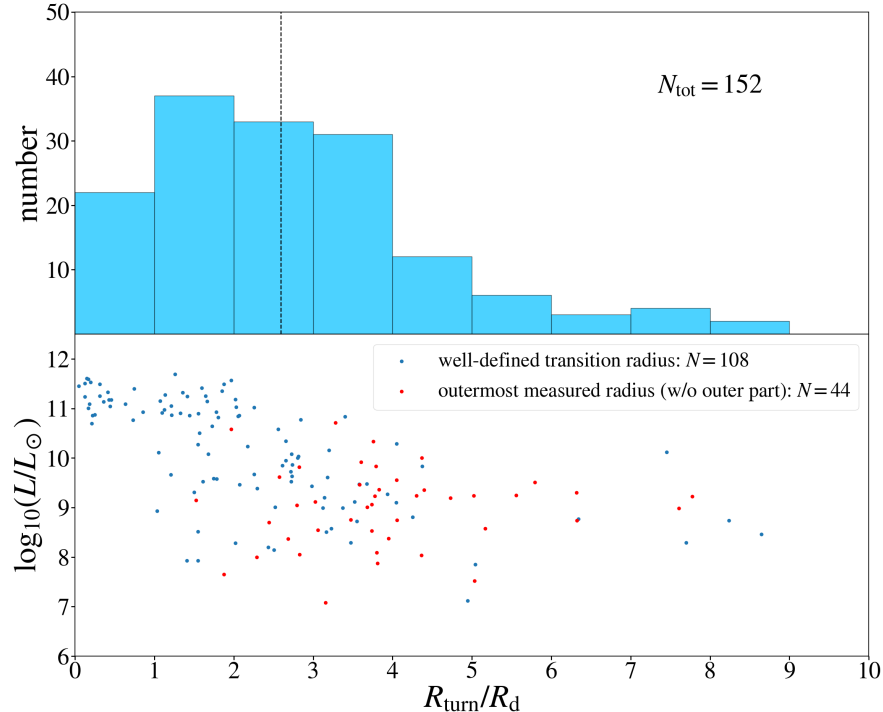


Figure 2. The upper panel shows the distribution of the inner-outer transition radius R_{turn} for 152 SPARC rotation curves used in this study. The vertical dotted line indicates the median value of $2.6R_d$ where R_d is the disk scale radius. The lower panel shows an anti-correlation of R_{turn}/R_d with galaxy infrared luminosity. Red dots indicate the outermost radii when the observed RC rises up to the last measured point so that the outer part is unobserved or ill-defined.

and a relatively small inner part while subluminal galaxies often have an RC rising over a large radial range. These trends are very similar if all 175 SPARC galaxies are used.

2.2. Methods

2.2.1. Λ CDM

For CDM, an MCMC modeling is used to fit the rotation curve of each galaxy using halo density profiles which are constrained by cosmological hydrodynamic simulations under the Λ CDM paradigm. A widely used functional form (Zhao 1996) to describe the halo is given by

$$\rho_{\text{halo}}(r) = \frac{\rho_s}{\left(\frac{r}{r_s}\right)^\gamma \left[1 + \left(\frac{r}{r_s}\right)^\alpha\right]^{(\beta-\gamma)/\alpha}}, \quad (4)$$

where r_s is the scale radius and ρ_s the scale density. The virial radius r_{200} of the halo is defined to be the radius within which the CDM density is equal to 200 times the critical density of the universe, while the concentration of the halo is defined to be $c_{200} \equiv r_{200}/r_s$. The halo virial mass M_{200} is defined to be the mass within r_{200} . Parameters γ and β control the inner and outer density slopes while parameter α controls the sharpness of the inner-outer transition. The parameter choice $(\alpha, \beta, \gamma) = (1, 3, 1)$ is the Navarro-Frenk-White (NFW) profile (Navarro et al. 1997) which is the prediction of N-body simulations of CDM without any baryonic physics.

Recent cosmological hydrodynamic simulations of galaxy formation within CDM halos predict diverse (stellar to halo mass ratio M_*/M_{200} -dependent) DM density profiles (Di Cintio et al. 2014b; Dekel et al. 2017; Lazar et al. 2020) modified from the NFW profile due to baryonic feedback (e.g. Gnedin & Zhao 2002; Pontzen & Governato 2012). These results provide constraints on (α, β, γ) . Two specific cases are considered here.

One is the choice $(\alpha, \beta) = (0.5, 3.5)$ preferred by Dekel et al. (2017) based on the Numerical Investigation of Hundred Astrophysical Objects (NIHAO) simulations. In this case there are 3 free parameters which are chosen to be M_{200} , c_{200} and γ . (Note that M_{200} and c_{200} are used instead of r_s and ρ_s .) In MCMC, two prior constraints are imposed:

the popular halo mass-stellar mass abundance matching relation (Behroozi et al. 2013; Kravtsov et al. 2018) and the M_*/M_{200} -dependent slope estimated between radii $0.01r_{200}$ and $0.02r_{200}$ from the NIHAO simulations (Tollet et al. 2016).

The other case, dubbed as the DC14 model (Di Cintio et al. 2014b), provides constraints on all three indices (α, β, γ) and the concentration c_{200} . In this case, all five halo parameters M_{200} , c_{200} , α , β , and γ are allowed to vary with five prior constraints (including the M_{200} - M_* abundance matching relation) imposed on them.

Another functional form of DM halos considered here is the “core-Einasto profile” proposed recently based on the Feedback In Realistic Environments (FIRE)-2 galaxy formation simulations (Lazar et al. 2020). The FIRE-2 simulations provide a constraint on core size as a function of the stellar-to-halo mass ratio. See Appendix A for the details.

2.2.2. MOND

For MOND interpreted as modified gravity, the “Aquadatic Lagrangian (AQUAL)” theory field equation

$$\nabla \cdot [\mu(|\nabla\Phi|/a_0)\nabla\Phi] = 4\pi G\rho_{\text{bar}} \quad (5)$$

is numerically solved for the MOND potential Φ from which follows the radial acceleration $g_R = |\partial\Phi/\partial R|$. Here a_0 is the MOND critical acceleration measured to be $\simeq 1.2 \times 10^{-10} \text{ms}^{-2}$ and $\mu(x)$ is the MOND interpolating function (IF) which is assumed to take the simple form $x/(1+x)$ (Famaey & Binney 2005).³ First, a numerical solution of Equation (5) for a flattened system under a constant external field, given as (Chae & Milgrom 2022)

$$g_{\text{MOND}} = g_{\text{bar}}\nu(y_{1.1}) \left[1 + \tanh\left(\frac{1.1e_{\text{N}}}{g_{\text{bar}}/a_0}\right)^{1.2} \frac{\hat{\nu}(y_{1.1})}{3} \right], \quad (6)$$

where $y_{1.1} \equiv \sqrt{(g_{\text{bar}}/a_0)^2 + (1.1e_{\text{N}})^2}$, $\nu(y) = 0.5 + \sqrt{0.25 + y^{-1}}$, and $\hat{\nu}(y) \equiv d\ln\nu(y)/d\ln y$, is fitted to the stacked data from the outer rotation curves. This equation has the right asymptotic limits if the external field dominates over the internal field (c.f. equation (23) of Zonoozi et al. 2021). From this fit, the mean Newtonian external field strength is estimated to be $g_{\text{N,ext}} \approx 6.7 \times 10^{-3}a_0$ or $\tilde{e} \equiv \sqrt{g_{\text{N,ext}}/a_0} = 0.082^{+0.013}_{-0.018}$ (Chae et al. 2022). \tilde{e} is equivalent to the MOND external field in units of a_0 to a good approximation because $\tilde{e} \ll 1$. Then, under the mean value $\tilde{e} = 0.082$ (Chae et al. 2022), Equation (5) is solved (Chae & Milgrom 2022) for ρ_{bar} of each galaxy with a stellar disk and a gas disk (and a bulge if present) to predict an RAR for each galaxy. The details can be found in Appendix A.8. Finally, all simulated RARs are stacked and then are assigned the actual SPARC data uncertainties to get simulated ($g_{\text{bar}}, g_{\text{obs}}$). In addition to these simulated RARs, MCMC fitting results are considered for a subset of galaxies whose outer rotation curves have large dynamic ranges (Chae et al. 2022).

3. RESULTS

3.1. Dark matter

Figure 3 shows the MCMC fit results for three DM halo models and compares them with the SPARC data assuming mass-to-light ratios at a wavelength of $3.6\mu\text{m}$ of $\Upsilon_{\text{disk}} = 0.5\Upsilon_{\odot}$ for the disk, and $\Upsilon_{\text{bulge}} = 0.7\Upsilon_{\odot}$ for the bulge if present. The DM halo fitted results are roughly similar to the SPARC RAR but have larger scatters. (Relatively speaking, the DC14 model matches the SPARC RAR better than the other halo models.) Figure 3(B) further shows the binned medians of orthogonal residuals from the algebraic MOND relation (i.e., the interpolating function represented by the red curve). The medians are estimated through a Monte Carlo method using individual Gaussian widths for $\log_{10}g_{\text{bar}}$ and $\log_{10}g_{\text{obs}}$ that incorporate all uncertainties including mass-to-light ratios. The trend of medians deviates systematically from the SPARC median in all three cases. In particular, in the high and/or low acceleration limits the models deviate outside the expected range estimated conservatively based on 20 percent systematic variations in mass-to-light ratios. In fact, some galaxy-to-galaxy scatter in Υ_{disk} and Υ_{bulge} is expected, but the uncertainty of the median is less than 5 percent (Schombert et al. 2022).

Considering that hydrodynamic simulations may be less accurate for massive galaxies due to central black holes (Maccio et al. 2020) and reported rotation velocities can be less accurate in the central region if a bulge is present,

³ See Chae et al. (2019) for why this IF is a good approximation for the acceleration range of RCs.

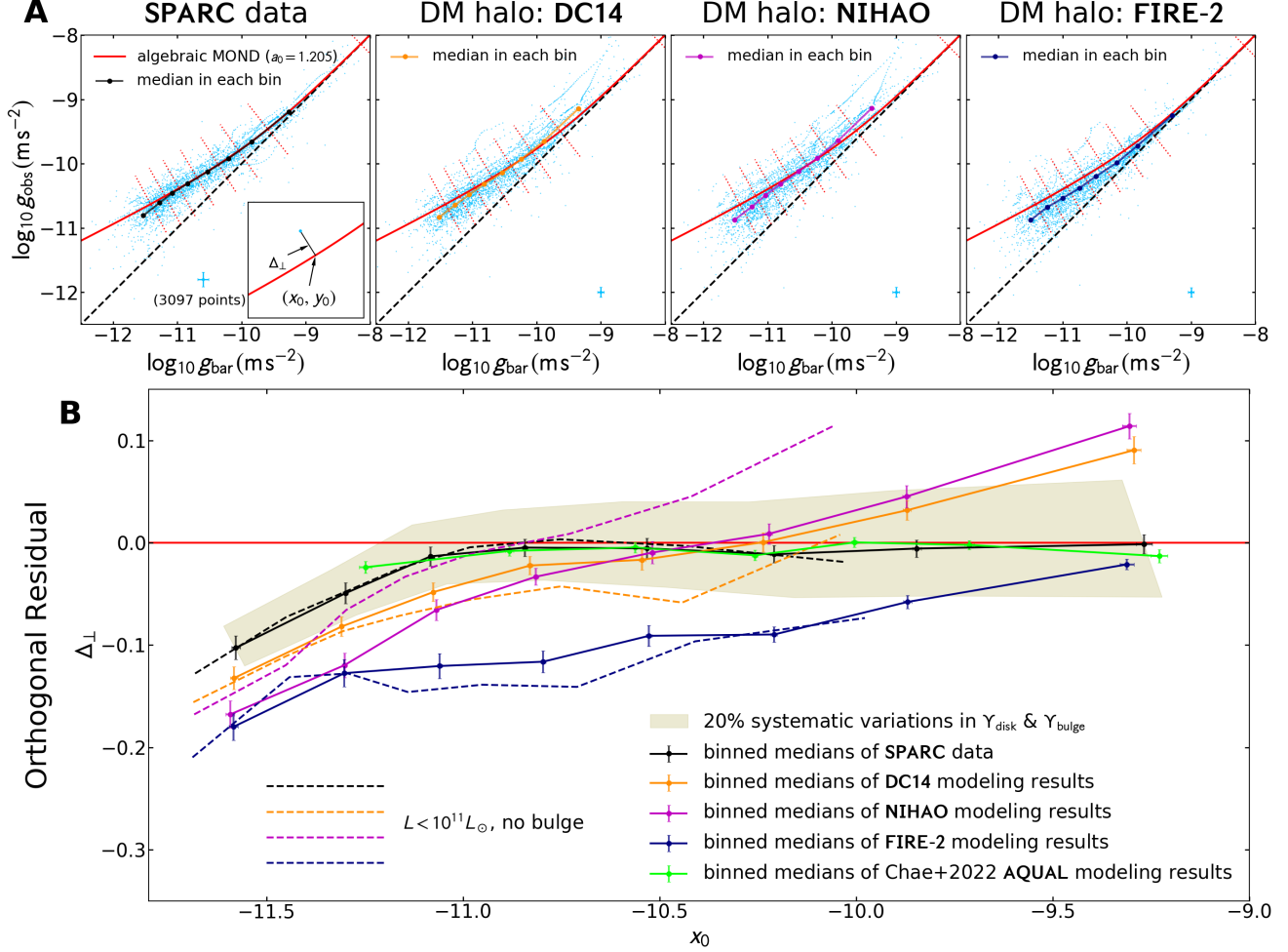


Figure 3. Comparison of MCMC fit results for two DM halo models with SPARC data. (A) Leftmost panel shows the SPARC data of 3097 points from 152 galaxies with mass-to-light ratios $\Upsilon_{\text{disk}} = 0.5\Upsilon_{\odot}$ for the disk and $\Upsilon_{\text{bulge}} = 0.7\Upsilon_{\odot}$ for the bulge. Typical uncertainties of the logarithm of accelerations are indicated by errorbars in the bottom of the panel. The inset defines the orthogonal residual Δ_{\perp} from the algebraic MOND relation, i.e., the interpolating function, for $a_0 = 1.205 \times 10^{-10} \text{ms}^{-2}$ fitted to the outer rotation curves. The other panels show MCMC fit results for the DC14 (Di Cintio et al. 2014a,b), NIHAO (Tollet et al. 2016; Dekel et al. 2017) and FIRE-2 (Lazar et al. 2020) models for hypothetical CDM halos. (B) This panel shows the trend of the medians of orthogonal residuals in the orthogonal bins. DM halo models systematically deviate from the SPARC data, in contrast to the AQUAL model (Chae et al. 2022). Dashed lines are results for a subsample of 111 galaxies without a bulge and with luminosity $L < 10^{11} L_{\odot}$, which reduces the role of BH feedback.

we also consider a subsample of 111 galaxies with luminosities $L < 10^{11} L_{\odot}$ and without a reported bulge. The results are represented by dashed lines in Figure 3(B). The results are somewhat shifted for some acceleration ranges with the DC14 and NIHAO models, but the shifted results are still discrepant with the SPARC data. Moreover, as will be shown below, if a rotation curve is separated into the inner rising and the outer quasi-flat parts, it is even harder to match the separated RARs by these DM models. On the other hand, the MCMC results (Chae et al. 2022) for the EFE-incorporated MOND models match well the SPARC pattern of orthogonal residuals – a recent AQUAL result is shown in Figure 3(B).

3.2. Modified gravity and modified inertia

Modified gravity and modified inertia can be distinguished by comparing the inner rising part and the outer quasi-flat part of rotation curves in the acceleration space. Modified gravity predicts an EFE-unrelated systematic deviation of the inner rising part (Brada & Milgrom 1995; Angus et al. 2012; Chae & Milgrom 2022) from the algebraic MOND

relation in axisymmetric flattened systems while modified inertia does not for circular orbits in axisymmetric systems (Milgrom 1994). Figure 4(A) shows the data separately for the inner and outer parts of the 152 SPARC galaxies and compare them with the predictions of AQUAL. The inner and outer parts are clearly distinguished, in agreement with the prediction of AQUAL. The difference between the inner and outer parts can also be quantified by the parameter \tilde{e} of Equation (6) fitted to the data points of each part. The MCMC fit (Chae et al. 2022) returns $\tilde{e} = 0.082_{-0.018}^{+0.013}$ with $a_0 = 1.205_{-0.033}^{+0.034} \times 10^{-10} \text{ms}^{-2}$ (outer) and $\tilde{e} = 0.157_{-0.007}^{+0.007}$ with $a_0 = 1.105_{-0.048}^{+0.050} \times 10^{-10} \text{ms}^{-2}$ (inner). The inferred values of a_0 are consistent, but the inferred \tilde{e} values show a 5.1σ difference. The orthogonal residual of the inner part of the SPARC data with respect to the algebraic MOND relation (-0.031 ± 0.004) is also $\approx 5\sigma$ different from that of the outer part (-0.010 ± 0.002) as shown in Figure 4(B). The AQUAL-predicted residuals are consistent with these SPARC residuals. The higher estimated \tilde{e} in the inner region can be thought of as arising from the vertical gravity just outside the disk plane, if we treat the disk as infinitely thin (Banik et al. 2018).

Figure 4(C) further illustrates the trend of the binned medians of orthogonal residuals for each part of the RCs. This clearly shows the difference between the inner and outer parts. This panel also includes AQUAL MCMC fit results for 65 galaxies whose outer parts were fitted with Equation (6) in a recent study (Chae et al. 2022). For the outer part, the deviation of the SPARC data for $x_0 \leq -11$ is consistent with the AQUAL EFE for an external field strength $\tilde{e} \lesssim 0.1$, where x_0 is the $x(\equiv \log_{10} g_{\text{bar}})$ value of the point projected on the algebraic MOND curve as defined in the figure. For the inner part, the trend of the SPARC data is consistent with the AQUAL prediction and MCMC fit results. Note that the MCMC fitted galaxies are relatively more massive and larger so that the inner data cover only $x_0 \geq -10.5$.

Figure 4(C) also shows the DC14 modeling results for 111 bulgeless galaxies with $L < 10^{11} L_{\odot}$, which is the most favorable CDM case among those shown in Figure 3. The outer part of the DC14 model deviates from the SPARC outer RAR at a significance of $\approx 3\sigma$ in terms of fitting the data with Equation (6). Moreover, the inner part deviates by a larger amount from the SPARC inner RAR.

3.3. MCMC fit of an AQUAL model to stacked data points of rotation curves

The stacked data ($\log_{10} g_{\text{bar}}, \log_{10} g_{\text{obs}}$) shown in Figure 4 are fitted by Equation (6) through a Bayesian MCMC method introduced (and applied to the outer data) by Chae et al. (2022). Figure 5 shows the PDFs and contour plots of parameters \tilde{e} and a_0 for three sets of data points: all points, the points only from the outer part, and the points only from the inner part. These PDFs clearly show that only the value $\tilde{e} = 0.082_{-0.018}^{+0.013}$ for the outer points is consistent with the value $\tilde{e} = 0.071$ (the magenta vertical line) from the large-scale distribution of baryonic matter in the local universe (Chae et al. 2021). The unacceptably large value $\tilde{e} = 0.157 \pm 0.007$ for the inner points cannot be due to the EFE. Moreover, the inferred \tilde{e} for the inner points is somewhat larger if we fix a_0 to the value inferred from the outer points. This is because the weaker gravity g_{obs} in the inner parts can be partly accounted for in the fit through a lower a_0 than for the outer data. *These results agree only with the predictions of modified gravity.*

The results shown in Figure 5 are for all 152 galaxies selected for this work. Because reported rotation velocities in the inner regions of massive spiral galaxies having a bulge can be less accurate due to the velocity dispersion in the bulge, we also consider a subsample of 111 galaxies without a detected bulge and luminosity $L < 10^{11} L_{\odot}$. Figure 6 shows the results. The difference between the inner and outer parts remains nearly the same. Also, the fitted value of $\tilde{e} = 0.073_{-0.028}^{+0.016}$ for the outer data points is now in even better agreement with the expected value from the cosmic environment.

4. DISCUSSION AND CONCLUSIONS

Modified gravity represented by the AQUAL theory can naturally explain both the inner and outer RARs of the SPARC data with a plausible mean external field strength. Various CDM halo models predicted by recent state-of-the-art hydrodynamic simulations do not reproduce well the total RAR or the inner-outer separated RARs. In particular, the inner part of CDM results is clearly discrepant with the SPARC inner RAR, even if excluding massive galaxies with a bulge for which BH feedback and measurement errors of rotation velocities are possible concerns. Considering the wide range of halo models tested here, it is unclear whether revised CDM galaxy formation models or alternative DM models such as self-interacting DM (Spergel & Steinhardt 2000) can provide a resolution. However, it is interesting to note that CDM predicts robustly that the inner RAR lies below the outer RAR as in the AQUAL prediction. Also, it is in principle possible that halo models can be fine-tuned to match the SPARC inner and outer RARs. What is surprising is that the AQUAL theory can match the RARs naturally without any fine-tuning.

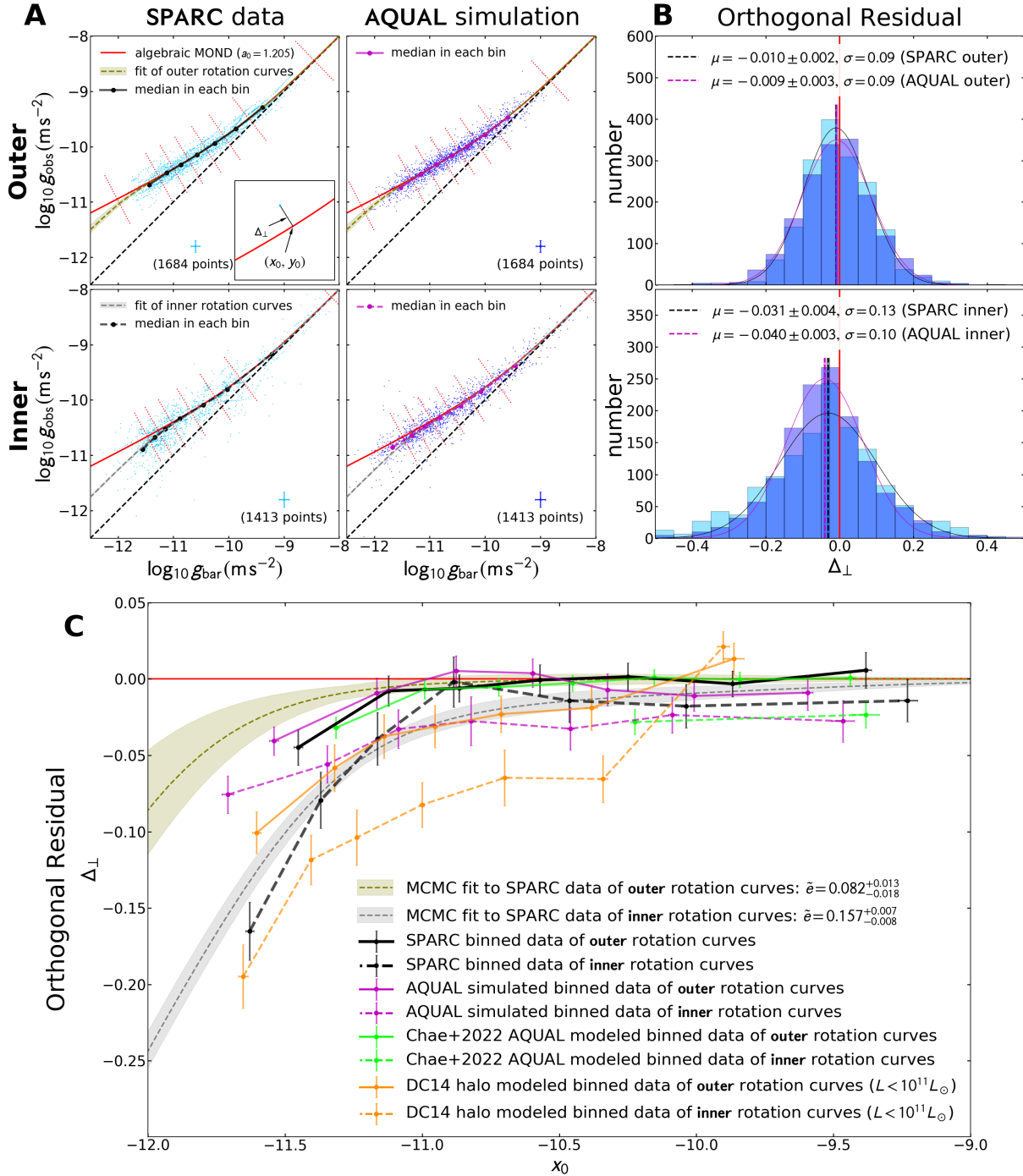


Figure 4. The inner and outer parts of rotation curves in acceleration space. (A) Each SPARC rotation curve shown in Figure 3(A) is separated into the inner rising and outer quasi-flat parts. Data for the two parts are displayed separately and compared with the AQUAL simulated results for the same galaxies. Each panel is in the same format as Figure 3(A). The dashed curve and band indicate the MCMC fit of Equation (6) to the SPARC data points of the inner or outer part. (B) Histograms show orthogonal residuals from the algebraic MOND relation (red line) for the outer (upper panel) and inner (lower panel) data points. Histograms are fitted with a Gaussian model, and the fitted mean μ (with a bootstrap error) and standard deviation σ are indicated. (C) Solid and dashed lines show the trend of orthogonal residuals in orthogonal bins for the outer and inner parts, respectively. Thick black lines represent the SPARC data while magenta lines represent the AQUAL simulated results. Green lines represent the MCMC fitted results for a subsample of 65 galaxies (Chae et al. 2022) of a good dynamic range that are relatively more massive and larger. Orange lines represent the DC14 results for 111 bulgeless galaxies with $L < 10^{11} L_{\odot}$, which is the most favorable CDM case shown in Figure 3.

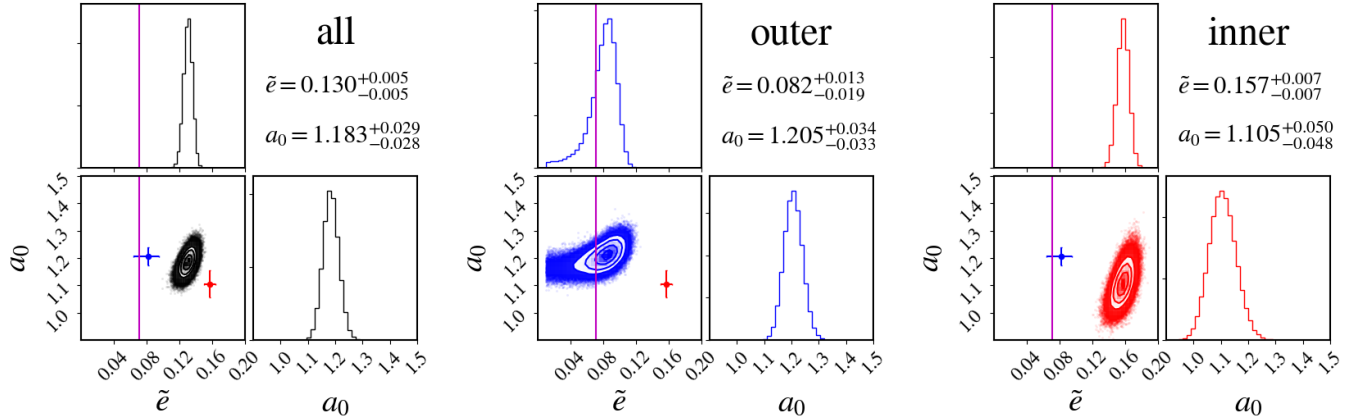


Figure 5. MCMC fit of the AQUAL model (Equation 6) to all data points (left), the outer RC data points (center), and the inner RC data points (right). Blue and red points with errorbars indicate the fitted values for the outer and inner parts, respectively. The difference in the fitted values of \tilde{e} for the inner and outer parts is evident, whereas the fitted a_0 values are consistent with each other. The magenta vertical line indicates the mean external field expected from the cosmic baryon distribution in the local universe (Chae et al. 2021, 2022), which is consistent only with the fitted \tilde{e} for the outer part.

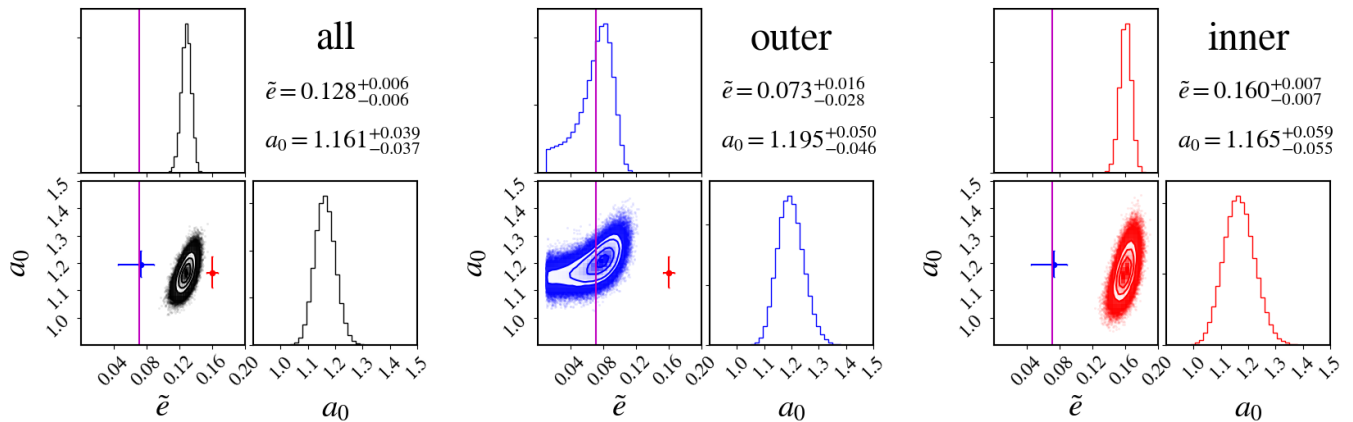


Figure 6. Same as Fig. 5 but for a subsample of 111 bulgeless galaxies with $L < 10^{11} L_{\odot}$. The difference between the inner and outer parts remains nearly the same.

The hypothesis that the inner and outer RARs follow a universal curve for axisymmetric systems is ruled out at 5σ significance based on the current SPARC database as demonstrated in Figure 4. Even if galaxies with a large luminosity ($L > 10^{11} L_{\odot}$) or a bulge are removed from the sample to minimize a possible systematic error, the shift between the inner and outer parts remains nearly the same. One may still consider a most conservative or pessimistic case that galaxies without a detected outer part (i.e. galaxies such as those in the bottom row of Figure 1)⁴ are removed further because they do not provide the *control* outer part within themselves. In this case, we are left with only 607 inner points and 680 outer points. For these relatively small samples \tilde{e} and a_0 cannot be constrained well simultaneously. Thus, if a canonical value of $a_0 = 1.20$ is assumed and only \tilde{e} is fitted, the two samples give $\tilde{e} = 0.141^{+0.011}_{-0.011}$ (inner) and $\tilde{e} = 0.074^{+0.013}_{-0.019}$ (outer). These values differ by $\approx 3.9\sigma$. This is a somewhat weaker difference than that for the full sample but still very significant.

Sanders (2019) considered a carefully selected 12 gas-dominated galaxies. Because these galaxies are heavily gas-dominated, they are free from usual uncertainties in the mass-to-light ratio of stellar disks. The Sanders (2019) RCs provide data points of the inner part in the context of this study. When one examines the Sanders (2019) RCs along

⁴ These are mostly late-type dwarf galaxies.

with the overplotted MOND predictions based on the so-called standard IF (rather than the simple IF, or the SPARC RAR, as used here and in the current literature in general), it seems at first sight that the inner points lie, in most cases, well on the algebraic MOND. If this is the case, it would support modified inertia contradicting the results of this study. However, because the standard IF predicts a weaker gravity for $0.1 \lesssim g_{\text{bar}}/a_0 \lesssim 10$ (see, e.g., figure 1 of [Chae et al. 2019](#)) than the one used in this study, the apparent agreement with the standard IF implies actually that the inner RCs are a little lower than the algebraic MOND represented by the simple IF. Since [Sanders \(2019\)](#) did not test quantitatively his selected RCs in the context of distinguishing between modified inertia and modified gravity, it is interesting to consider a similar sample selected using the [Sanders \(2019\)](#) criteria from the SPARC database. By requiring that the gas mass is at least 2.2 times larger than the stellar mass and the inclination is in the range $40^\circ \leq i < 80^\circ$, we are left with 28 gas-dominated galaxies that provide 331 inner data points. It is found that these data points lie below the algebraic MOND in the average/median sense and the fitting results in $\tilde{e} = 0.156_{-0.007}^{+0.007}$ (for a fixed $a_0 = 1.2$ because the data points do not provide high-acceleration data points), which is indistinguishable from the value for the total sample shown in Figure 5.

A recent analysis of 15 dwarf galaxies to distinguish between modified inertia and modified gravity ([Petersen & Lelli 2020](#)) based on a dimensionless global parameter ([Milgrom 2012](#)) obtained a marginal preference for modified gravity. This work clearly shows that modified gravity is preferred over modified inertia. Ironically, if the current SPARC database suffered from a gross systematic error so that the inner and outer RARs were universal, both CDM and modified gravity would be ruled out and modified inertia would be favored. However, as shown above the current SPARC database clearly prefers modified gravity represented by the AQUAL theory over modified inertia or CDM.

When the SPARC database was analyzed by [Chae et al. \(2020, 2021\)](#) with an analytic spherical MOND model from [Famaey & McGaugh \(2012\)](#), it was a surprise that external fields inferred from internal dynamics based on such a simple model agreed with those expected from cosmic environments. Those previous studies called for further studies based on more accurate and realistic modeling ([Chae & Milgrom 2022; Chae et al. 2022](#)). Now that the inner and outer parts of RCs are separated and numerical solutions of modified gravity are used here, the EFE interpretation of SPARC RCs is upheld. In this regard, it is interesting to note a recent study supporting EFE in dwarf (spheroidal and elliptical) galaxies of the Fornax Cluster ([Asencio et al. 2022](#)). It shows that the EFE from the cluster needs to be considered when finding the tidal radii of the dwarf galaxies, as otherwise they would have a lot more self-gravity, making them immune to tides, thus contradicting observations. In conclusion, EFE is empirically supported by currently observed galaxies and its origin is likely to be modified gravity rather than modified inertia.

ACKNOWLEDGMENTS

The author thanks S. McGaugh, F. Lelli and J. Schombert for the help with understanding the SPARC database, and M. Milgrom for insightful communications. It is the author's pleasure to acknowledge a very useful anonymous report that helped improve the presentations significantly. This work was supported by National Research Foundation of Korea (grant No. NRF-2019R1F1A1062477).

REFERENCES

- Abdalla, E., et al. 2022, JHEA, 34, 49
- Angus, G. W., van der Heyden, K. J., B. Famaey, Gentile, G., McGaugh, S. S., de Blok, W. J. G. 2012, MNRAS, 421, 2598
- Asencio, E., Banik, I., Mieske, S., Venhola, A., Kroupa, P., Zhao, H. 2022, MNRAS, 515, 2981
- Banik, I., Nagesh, S. T., Haggi, H., Kroupa, P., Zhao, H. 2022, MNRAS, 513, 3541
- Banik, I., Milgrom, M., Zhao, H. 2018, arXiv:1808.10545
- Banik, I., Zhao, H. 2022, Symmetry, 14, 1331
- Behroozi, P. S., Wechsler, R. H., Conroy, C. 2013, ApJ, 770, 57
- Bekenstein, J., Milgrom, M. 1984, ApJ, 286, 7
- Blumenthal, G. R., Faber, S. M., Primack, J. R., Rees, M. J. 1984, Nature, 311, 517
- Brada, R., Milgrom, M. 1995, MNRAS, 276, 453
- Brook, C. B., Stinson, G., Gibson, B. K., Wadsley, J., Quinn, T. 2012, MNRAS, 424, 1275
- Bryan, G. L., Norman, M. L. 1998, ApJ, 495, 80
- Bull, P., et al. 2016, PDU, 12, 56
- Bullock, J. S., Boylan-Kolchin, M. 2017, ARA&A, 55, 343
- Chae, K.-H., Bernardi, M., Sheth, R. K., Gong, I.-T. 2019, ApJ, 877, 18
- Chae, K.-H., Desmond, H., Lelli, F., McGaugh, S. S., Schombert, J. M. 2021, ApJ, 921, 104

- Chae, K.-H., Lelli, F., Desmond, H., McGaugh, S. S., Li, P., Schombert, J. M. 2020, *ApJ*, 904, 51
- Chae, K.-H., Lelli, F., Desmond, H., McGaugh, S. S., Schombert, J. M. 2022, *PhRvL*, submitted
- Chae, K.-H., Milgrom, M. 2022, *ApJ*, 928, 24
- Dekel, A., Ishai, G., Dutton, A. A., Maccio, A. V. 2017, *MNRAS*, 468, 1005
- Desmond, H. 2017, *MNRAS*, 464, 4160
- Di Cintio, A., Brook, C. B., Maccio, A. V., Stinson, G. S., Knebe, A. 2014b, *MNRAS*, 441, 2986
- Di Cintio, A., Brook, C. B., Maccio, A. V., Stinson, G. S., Knebe, A., Dutton, A. A., Wadsley, J. 2014a, *MNRAS*, 437, 415
- Di Cintio, A., Lelli, F. 2016, *MNRAS*, 456, L127
- Di Valentino, E., Mena, O., Pan, S., Visinelli, L., Yang, W., Melchiorri, A., Mota, D. F., Riess, A. G., Silk, J. 2021, *CQG*, 38, 153001
- Dutton, A. A., Maccio, A. V. 2014, *MNRAS*, 441, 3359
- Famaey, B., Binney, J. 2005, *MNRAS*, 363, 603
- Famaey, B., McGaugh, S. S. 2012, *LRR*, 15, 10
- Foreman-Mackey, D., Hogg, D. W., Lang, D., Goodman, J. 2013, *PASP*, 125, 306
- Gnedin, O. Y., Zhao, H. 2002, *MNRAS*, 333, 299
- Hernquist, L. 1990, *ApJ*, 356, 359
- Katz, H., Lelli, F., McGaugh, S. S., Di Cintio, A., Brook, C. B., Schombert, J. M. 2017, *MNRAS*, 466, 1648
- Keller, B. W., Wadsley, J. W. 2017, *ApJ*, 835, L17
- Kravtsov, A. V., Vikhlinin, A. A., Meshcheryakov, A. V. 2018, *AstL*, 44, 8
- Kroupa, P. 2012, *PASA*, 29, 395
- Lazar, A., Bullock, J. S., Boylan-Kolchin, M., Chan, T. K., Hopkins, P. F., Graus, A. S., Wetzel, A., El-Badry, K., Wheeler, C., Straight, M. C., Keres, D., Faucher-Giguere, C.-A., Fitts, A., Garrison-Kimmel, S. 2020, *MNRAS*, 497, 2393
- Lelli, F., McGaugh, S. S., Schombert, J. M. 2016, *AJ*, 152, 157
- Li, P., Lelli, F., McGaugh, S. S., Schombert, J. M. 2020, *ApJS*, 247, 31
- Li, P., McGaugh, S. S., Lelli, F., Tian, Y., Schombert, J. M., Ko, C.-M. 2022, *ApJ*, 927, 198
- Ludlow, A. D., Benitez-Llambay, A., Schaller, M., Theuns, T., Frenk, C. S., Bower, R., Schaye, J., Crain, R. A., Navarro, J. F., Fattahi, A., Oman, K. A. 2017, *PhRvL*, 118, 161103
- Maccio, A. V., Crespi, S., Blank, M., Kang, X. 2020, *MNRAS*, 495, L46
- Maccio, A. V., Dutton, A. A., van den Bosch, F. C. 2008, *MNRAS*, 391, 1940
- McGaugh, S. S. 2005, *ApJ*, 632, 859
- McGaugh, S. S., Lelli, F., Schombert, J. M. 2016, *PhRvL*, 117, 201101
- McGaugh, S. S., Lelli, F., Schombert, J. M. 2020, *RNAAS*, 4, 45
- Milgrom, M. 1983a, *ApJ*, 270, 365
- Milgrom, M. 1983a, *ApJ*, 270, 371
- Milgrom, M. 1986, *ApJ*, 302, 617
- Milgrom, M. 1984, *Ann. Phys.*, 229, 384
- Milgrom, M. 1999, *PLA*, 253, 273
- Milgrom, M. 2010, *MNRAS*, 403, 886
- Milgrom, M. 2012, *PhRvL*, 109, 251103
- Milgrom, M. 2022, *arXiv:2208.07073*
- Miyamoto, M., Nagai, R. 1975, *PASJ*, 27, 533
- Navarro, J. F., Benitez-Llambay, A., Fattahi, A., Frenk, C. S., Ludlow, A. D., Oman, K. A., Schaller, M., Theuns, T. 2017, *MNRAS*, 471, 1841
- Navarro, J. F., Frenk, C. S., White, S. D. M., *ApJ*, 490, 493
- Oria, P.-A., Famaey, B., Thomas, G. F., Ibata, R., Freundlich, J., Posti, L., Korsaga, M., Monari, G., Müller, O., Libeskind, N. I., Pawlowski, M. S. 2021, *ApJ*, 923, 68
- Paranjape, A., Sheth, R. K. 2021a, *MNRAS*, 507, 632
- Paranjape, A., Sheth, R. K. 2021b, *arXiv:2112.00026*
- Peebles, P. J. E. 1982, *ApJ*, 263, L1
- Peebles, P. J. E. 2022, *arXiv:2208.05018*
- Perivolaropoulos, L., Skara, F. 2022, *New Ast. Rev.*, 95, 101659 (*arXiv:2105.05208*)
- Petersen, J., Lelli, F. 2020, *A&A*, 636, A56
- Pontzen, A., Governato, F. 2012, *MNRAS*, 421, 3464
- Sanders, R. H. 2019, *MNRAS*, 485, 513
- Schombert, J. M., McGaugh, S. S., Lelli, F. 2022, *AJ*, 163, 154
- Smith, R., Flynn, C., Candlish, G. N., Fellhauer, M., Gibson, B. K. 2015, *MNRAS*, 448, 2934
- Spergel, D. N., Steinhardt, P. J. 2000, *PhRvL*, 84, 3760
- Stinson, G. S., Brook, C., Maccio, A. V., Wadsley, J., Quinn, T. R., Couchman, H. M. P. 2013, *MNRAS*, 428, 129
- Tenneti, A., Mao, Y.-Y., Croft, R. A. C., Di Matteo, T., Kosowsky, A., Zago, F., Zentner, A. R. 2018, *MNRAS*, 474, 3125
- Tollet, E., Maccio, A. V., Dutton, A. A., Stinson, G. S., Wang, L., Penzo, C., Gutcke, T. A., Buck, T., Kang, X., Brook, C., Di Cintio, A., Keller, B. W., Wadsley, J. 2016, *MNRAS*, 456, 3542
- White, S. D. M., Rees, M. J. 1978, *MNRAS*, 183, 341
- Zhao, H. 1996, *MNRAS*, 278, 488
- Zonoozi, A. H., Lieberz, P., Banik, I., Haggi, H., Kroupa, P. 2021, *MNRAS*, 506, 5468

APPENDIX

A. METHODS

A.1. MCMC modeling

A Bayesian approach is used to fit a model to the observed the rotation curve of a galaxy. The method is essentially the same as that adopted in [Chae et al. \(2022\)](#) in their MOND modeling. Here both DM halo and MOND models are considered. A likelihood \mathcal{L} for a given model with free parameters $\boldsymbol{\beta} = \{\beta_k\}$, which includes inclination i , is defined as⁵

$$\ln \mathcal{L} = -\frac{1}{2} \sum_{j=1}^N \left[\left(\frac{V_{\text{rot}}(i; R_j) - V_{\text{mod}}(\boldsymbol{\beta}; R_j)}{\sigma_{V_{\text{rot}}}(i; R_j)} \right)^2 + \ln \left(2\pi\sigma_{V_{\text{rot}}}(i; R_j) \right) \right], \quad (\text{A1})$$

where $V_{\text{rot}}(i; R_j) = V_{\text{obs}}(R_j) \sin(i_{\text{obs}}) / \sin(i)$, $\sigma_{V_{\text{rot}}}(i; R_j) = \sigma_{V_{\text{obs}}}(R_j) \sin(i_{\text{obs}}) / \sin(i)$, and $V_{\text{mod}}(\boldsymbol{\beta}; R_j)$ is the theoretical velocity that depends on the model. Then, the posterior probability of $\boldsymbol{\beta}$ is given by

$$p(\boldsymbol{\beta}) = \mathcal{L} \times \prod_k \text{Pr}(\beta_k), \quad (\text{A2})$$

where $\text{Pr}(\beta_k)$ is the prior probability of parameter β_k . (See below for prior constraints on inclination and other parameters.) With this definition of probability, the public MCMC package `emcee` ([Foreman-Mackey et al. 2013](#)) is used to derive the posterior probability density function (PDF) of the model parameters.

The theoretical rotation velocity $V_{\text{mod}}(\boldsymbol{\beta}; R_j)$ is defined under the DM or MOND hypothesis. Under the DM hypothesis, the theoretical velocity is defined as

$$V_{\text{mod}} = \sqrt{V_{\text{mod,bar}}^2 + V_{\text{mod,halo}}^2}, \quad (\text{A3})$$

where $V_{\text{mod,halo}}$ is the Newtonian velocity contributed by the DM halo model, and $V_{\text{mod,bar}}$ is the Newtonian velocity contributed by the observed baryons, which depends on some of the free parameters as

$$V_{\text{mod,bar}} = \sqrt{\hat{D}(\hat{\Upsilon}_{\text{disk}} V_{\text{disk}}^2 + \hat{\Upsilon}_{\text{bulge}} V_{\text{bulge}}^2 + \hat{\Upsilon}_{\text{gas}} V_{\text{gas}} |V_{\text{gas}}|)}, \quad (\text{A4})$$

where $\hat{D} \equiv D/D_{\text{obs}}$ is the parameter representing distance to the galaxy normalized by the SPARC reported distance D_{obs} , and $\hat{\Upsilon}_{\text{disk}}$, $\hat{\Upsilon}_{\text{bulge}}$ and $\hat{\Upsilon}_{\text{gas}}$ are the parameters representing galaxy-specific mass-to-light ratios and the gas-to-HI mass ratio normalized by 0.5, 0.7, and 1.33, respectively. Note that V_{gas} can make a negative contribution in some rare cases in the inner region of the galaxy due to deviations from spherical symmetry ([Lelli et al. 2016](#)).

Under the MOND hypothesis, the theoretical velocity is given by

$$V_{\text{mod}} = \sqrt{\frac{g_{\text{MOND}}}{g_{\text{bar}}}} V_{\text{bar}}, \quad (\text{A5})$$

where $g_{\text{MOND}}/g_{\text{bar}}$ specifies the MOND model and is given by Equation (6) in the case of AQUAL.

A.2. The approach of this work to CDM halos

A number of studies in the literature compared statistical properties of Λ CDM-simulated mock galaxies (e.g. [Di Cintio & Lelli 2016](#); [Keller & Wadsley 2017](#); [Ludlow et al. 2017](#); [Desmond 2017](#); [Navarro et al. 2017](#); [Tenneti et al. 2018](#); [Paranjape & Sheth 2021a,b](#)) with the SPARC RAR. Here we build halo models for actual SPARC galaxies based on recent hydrodynamic simulations of galaxy formation in Λ CDM. This approach is similar to that used in [Li et al. \(2020\)](#) where a number of halo models were built for SPARC galaxies. However, here only sophisticated halo models with constraints from recent hydrodynamic simulations are considered.

Current state-of-the-art hydrodynamic simulations of galaxy formation under the Λ CDM cosmological model predict density profiles of CDM halos. Here we need simulation results for relatively low-mass halos with $M_{\text{halo}} \lesssim 10^{13} M_{\odot}$

⁵ The second logarithmic term in the bracket was actually used by [Chae et al. \(2020\)](#) who however did not state it explicitly.

applicable to most SPARC galaxies. We consider results from three independent projects: the NIHAO series (Tollet et al. 2016; Dekel et al. 2017; Maccio et al. 2020), the DC14 analyses of their simulations (Di Cintio et al. 2014a,b), and the FIRE-2 simulation (Lazar et al. 2020). The details of these results are described below. The DC14 results were also used in a previous MCMC analysis of CDM halos (Katz et al. 2017). That study stressed that the DC14 model matched observed galaxies better than the NFW model based on DM only simulations. However, they did not test the DC14 model based on a statistical RAR (let alone the inner-outer separation of RCs) as done here.

A.3. CDM halo masses and radii

The radius of a halo denoted by r_{200} is defined as the radius within which the average mass density is 200 times the present-day critical density of the universe $\rho_{\text{crit},0} = 3H_0^2/(8\pi G)$, where H_0 is the Hubble constant. The mass of the halo denoted by M_{200} is the mass bounded by r_{200} . Then, the numerical value of r_{200} is given by

$$r_{200} = 0.02063 \left(\frac{M_{200}}{M_\odot} \right)^{1/3} h_{70}^{-2/3} \text{kpc}, \quad (\text{A6})$$

where $h_{70} \equiv H_0/(70 \text{ km s}^{-1} \text{ Mpc}^{-1})$. Throughout this work the value of H_0 is taken to be $73 \text{ km s}^{-1} \text{ Mpc}^{-1}$ and so $h_{70} = 73/70$.

Because some authors use different definitions of halo radius and mass than the above, we also consider virial radius and mass (r_{vir} and M_{vir}) from Bryan & Norman (1998). In this definition, the over-density factor for the halo region is about one half of 200, so that $r_{\text{vir}} \approx 1.4r_{200}$ and M_{vir} is accordingly related to M_{200} .

We use the popular abundance matching relation between halo mass M_{200} and stellar mass M_\star to provide a constraint on the halo. The following relation is taken from the literature

$$\log_{10} M_\star = \log_{10}(\epsilon M_1) + f \left[\log_{10} \left(\frac{M_{200}}{M_1} \right) \right] - f(0), \quad (\text{A7})$$

where the function $f(x)$ is defined as

$$f(x) = -\log_{10}(10^{-ax} + 1) + \frac{\delta[\log_{10}(1 + e^x)]^b}{1 + e^{10^{-x}}}. \quad (\text{A8})$$

We consider two results (Behroozi et al. 2013; Kravtsov et al. 2018) which bracket the current range. Behroozi et al. (2013) report $a = 1.412$, $b = 0.316$, $\delta = 3.508$, $\log_{10} M_1/M_\odot = 11.514$, and $\log_{10} \epsilon = -1.777$ while Kravtsov et al. (2018) report $a = 1.779$, $b = 0.547$, $\delta = 4.394$, $\log_{10} M_1/M_\odot = 11.35$, and $\log_{10} \epsilon = -1.642$. These two differ appreciably only for large masses $M_{200} \gtrsim 10^{12} M_\odot$. We will see below that the posterior M_{200} - M_\star relation is closer to the Kravtsov et al. (2018) relation, consistent with an earlier finding (Di Cintio & Lelli 2016). The parameter ρ_s in Equation (4) is determined by M_{200} .

A.4. Rotation velocity contributed by the halo

For a halo described by Equation (4), the halo contribution to the rotation velocity $V_{\text{mod,halo}}$ is given by

$$V_{\text{mod,halo}}(R) = 10^3 \left[\frac{4.3 M_{200}/(10^{12} M_\odot)}{R/\text{kpc}} \times \frac{f(c_{200} R/r_{200}, \alpha, \beta, \gamma)}{f(c_{200}, \alpha, \beta, \gamma)} \right]^{1/2} \text{km s}^{-1}, \quad (\text{A9})$$

with the definition

$$f(x, \alpha, \beta, \gamma) \equiv \int_0^x \frac{s^{2-\gamma}}{(1+s^\alpha)^{(\beta-\gamma)/\alpha}} ds. \quad (\text{A10})$$

In Equation (A9), we use the usual concentration parameter $c_{200} \equiv r_{200}/r_s$ although its meaning is different than that from dark matter only simulations. For the core-Einasto profile (Lazar et al. 2020), the integral function of Equation (A10) is modified accordingly.

A.5. Hydrodynamic simulation results on halo density profiles: NIHAO

An analysis of NIHAO halos (Dekel et al. 2017) found that the simple choice $(\alpha, \beta) = (0.5, 3.5)$ in Equation (4) can be as good as allowing them to be free in describing the simulated halos. Another analysis (Lazar et al. 2020) from the

NIHAO project measured the logarithmic slope between $r = 0.01r_{200}$ and $0.02r_{200}$. The reported logarithmic slope (multiplied by -1) over this radial range, denoted by γ_1 , is given as a function of $x \equiv M_*/M_{200}$ by

$$\gamma_1(x) = 0.158 + \log_{10} \left[26.49 \left(1 + \frac{x}{9.44 \times 10^{-5}} \right)^{-0.85} + \left(\frac{x}{8.77 \times 10^{-3}} \right)^{1.66} \right] \quad (\text{A11})$$

with a 1σ scatter of 0.18. Equation (A11) is used as a prior constraint on the halo profile.

In this model, the free parameters in Equation (A1) are $\beta = \{i, \hat{D}, \hat{\Upsilon}_{\text{disk}}, (\hat{\Upsilon}_{\text{bulge}}), \hat{\Upsilon}_{\text{gas}}, M_{200}, c_{200}, \gamma\}$. The priors on $i, \hat{D}, \hat{\Upsilon}_{\text{disk}}, \hat{\Upsilon}_{\text{bulge}}$, and $\hat{\Upsilon}_{\text{gas}}$ are the same as table 1 of Chae et al. (2020). Additional priors on the DM halo are provided by Equation (A7) and Equation (A11). In the case of Equation (A7), a lognormal prior on M_* ⁶ is imposed with a scatter of 0.25 dex.

A.6. Hydrodynamic simulation results on halo density profiles: DC14

A suite of cosmological hydrodynamic simulations called Making Galaxies In a Cosmological Context (MaGICC) (Brook et al. 2012; Stinson et al. 2013) provides a detailed prediction of the halo density profiles (Di Cintio et al. 2014b) affected by the baryonic physics of galaxy formation. The results presented by Di Cintio et al. (2014b) (DC14 model) predict the behaviors of all three shape indices α , β , and γ as functions of M_*/M_{vir} . They are

$$\begin{aligned} \alpha &= 2.94 - \log_{10}[(10^{X+2.33})^{-1.08} + (10^{X+2.33})^{2.29}], \\ \beta &= 4.23 + 1.34X + 0.26X^2, \\ \gamma &= -0.06 + \log_{10}[(10^{X+2.56})^{-0.68} + 10^{X+2.56}], \end{aligned} \quad (\text{A12})$$

where $X \equiv \log_{10}(M_*/M_{\text{vir}})$ and their definition of M_{vir} is the mass of a sphere within which the mass density is 93.6 times the critical density (typically $1.1M_{200} \lesssim M_{\text{vir}} \lesssim 1.4M_{200}$). These scaling relations are used as priors with a small scatter of 0.05. We also require $\alpha \geq 0.5$ because the simulation results do not actually include any value less than 0.5.

Furthermore, the DC14 model predicts how the scale radius r_s depends on a galaxy's star formation efficiency. The radius where the logarithmic slope of the density is -2 , to be denoted by r_{-2} , has the following scaling relation with the above-defined X for the simulated halos

$$\frac{c_{-2}}{c_{\text{NFW}}} = 1.0 + 0.00003e^{3.4(X+4.5)}, \quad (\text{A13})$$

where $c_{-2} \equiv r_{\text{vir}}/r_{-2} = (r_{\text{vir}}/r_s)[(2-\gamma)/(\beta-2)]^{-1/\alpha}$ and c_{NFW} is the concentration of the NFW halos from dark matter only simulations. For the NFW concentration we consider Dutton & Maccio (2014) based on the Planck cosmology which works slightly better than Maccio et al. (2008) based on the WMAP5 cosmology in matching the SPARC data. The Planck NFW concentration is given by

$$\log_{10}c_{\text{NFW}} = 0.905 - 0.101\log_{10} \left(\frac{M_{200}}{1.43 \times 10^{12} h_{70}^{-1} M_{\odot}} \right). \quad (\text{A14})$$

We use Equation (A13) along with Equation (A14) as a prior constraint with a lognormal scatter of 0.1. Thus, the DC14 model has free parameters $\beta = \{i, \hat{D}, \hat{\Upsilon}_{\text{disk}}, (\hat{\Upsilon}_{\text{bulge}}), \hat{\Upsilon}_{\text{gas}}, M_{200}, c_{200}, \alpha, \beta, \gamma\}$, with additional constraints provided by Equations (A12), (A13) and (A14). When these constraints are used, a proper transformation between M_{vir} (c_{vir}) and M_{200} (c_{200}) is used.

A.7. Hydrodynamic simulation results on halo density profiles: FIRE-2

The Feedback In Realistic Environments (FIRE)-2 simulation results (Lazar et al. 2020) have been fitted with the ‘‘core-Einasto’’ profile given as

$$\rho_{\text{cEin}}(r) = \tilde{\rho}_s \exp \left\{ -\frac{2}{\alpha_{\epsilon}} \left[\left(\frac{r+r_c}{\tilde{r}_s} \right)^{\alpha_{\epsilon}} - 1 \right] \right\}, \quad (\text{A15})$$

⁶ The stellar mass is obtained by $M_* = \hat{\Upsilon}_{\text{disk}}0.5(L_{\text{tot}} - L_{\text{bulge}}) + \hat{\Upsilon}_{\text{bulge}}0.7L_{\text{bulge}}$, where L_{tot} is the total luminosity and L_{bulge} is the luminosity of the bulge. The values of L_{bulge} are taken from the SPARC website: <http://astroweb.cwru.edu/SPARC/>.

where r_c and \tilde{r}_s are the core radius and scale radius defined for this profile. They find $\alpha_\epsilon = 0.16$ and a core radius as a function of the stellar-to-halo mass ratio given as

$$r_c(x) = 10^{A_1} \left(A_2 + \frac{x}{x_1^*} \right)^{-\beta_1} \left(\frac{x}{x_2^*} \right)^{\gamma_1} \text{ kpc} \quad (\text{A16})$$

where $x \equiv M_*/M_{\text{vir}}$, $A_1 = 1.21$, $A_2 = 0.71$, $x_1^* = 7.2 \times 10^{-3}$, $x_2^* = 0.011$, $\beta_1 = 2.31$, and $\gamma_1 = 1.55$. The FIRE-2 model has free parameters $\beta = \{i, \hat{D}, \hat{Y}_{\text{disk}}, (\hat{Y}_{\text{bulge}},) \hat{Y}_{\text{gas}}, M_{200}, \tilde{c}_{200}\}$, where $\tilde{c}_{200} \equiv r_{200}/\tilde{r}_s$. When Equation (A16) is used, a proper transformation between M_{vir} and M_{200} is applied.

A.8. AQUAL simulation

There are two nonrelativistic Lagrangian theories of MONDian modified gravity that can be used to model the galactic rotation curve of a rotationally supported galaxy. They are the AQUAL (Bekenstein & Milgrom 1984) and QUMOND (Milgrom 2010) field equations. These modified Poisson's equations are nonlinear and must be solved numerically. Solutions of the field equations are unusually difficult when an external field is present in an arbitrary direction. Recently, Chae & Milgrom (2022) have investigated numerical solutions of both the AQUAL and QUMOND field equations when an external field is either aligned or inclined with the rotation axis of disks with different thickness. QUMOND numerical solutions were also investigated by other researchers (Zonoozi et al. 2021; Oria et al. 2021).

Chae et al. (2022) tested AQUAL and QUMOND theories by comparing an external field fitted to the stacked data of the outer part of rotation curves of 114 SPARC galaxies⁷ with a cosmic mean external field estimated directly from observations of the local universe (Chae et al. 2021). Chae et al. (2022) finds that AQUAL is preferred over QUMOND by the outer part of rotation curves. The AQUAL fitted value of the mean external field strength is $\tilde{e} = 0.082_{-0.018}^{+0.013}$, which is consistent with the value $\tilde{e} = 0.071 \pm 0.001$ (Chae et al. 2021) from the environment for the case that all intergalactic baryons are maximally correlated with visible galaxies (their ‘‘max clustering’’ case). Thus, in this work simulations are carried out under the AQUAL theory with $\tilde{e} = 0.082$.

A galaxy is represented by a combination of a stellar disk, a gas disk, and a bulge if present. The base model for a disk is the Miyamoto-Nagai (MN; Miyamoto & Nagai 1975) model whose normalized mass distribution is given by

$$\rho_{\text{MN}}(R, z) = \frac{b^2 a R^2 + (a + 3\sqrt{z^2 + b^2})(a + \sqrt{z^2 + b^2})^2}{4\pi [R^2 + (a + \sqrt{z^2 + b^2})^2]^{5/2} (z^2 + b^2)^{3/2}}, \quad (\text{A17})$$

where a and b are the MN scale parameters in the radial and vertical directions. The stellar disk is represented by an approximate exponential disk with a finite thickness composed of three MN models (Smith et al. 2015). The effective mass density of this disk composed of three MN components may be approximated by a double exponential model

$$\rho_{\text{disk}}(R, z) = \rho_0 \exp(-R/R_d) \exp(-|z|/h_z), \quad (\text{A18})$$

where R_d and h_z are the scale radius and height. Three MN models have different values of a but share a common value of b . For $b/R_d \ll 1$, the scale height is related to b by $h_z \approx 0.8b$. For the model disk we choose $b/R_d = 0.1$ so that $h_z/R_d \approx 0.08$ consistent with observations of typical disk galaxies⁸. The gas disk is simply represented by a single MN model with $a = 2R_d$ and $b = 0.1a$.

The bulge is represented by the Hernquist model (Hernquist 1990):

$$\rho_{\text{H}}(r) = \frac{M_{\text{bulge}} r_{\text{H}}}{2\pi r (r + r_{\text{H}})^3}, \quad (\text{A19})$$

where r_{H} is the Hernquist scale radius. Following Li et al. (2022) we use the empirical relation

$$\log_{10}(r_{\text{H}}) = 1.29 \log_{10}(R_d) - 0.77. \quad (\text{A20})$$

The mass of the stellar disk ($M_{\text{★disk}}$) is given by $M_{\text{★disk}}/M_{\odot} = 0.5(L_{\text{tot}} - L_{\text{bulge}})/L_{\odot}$, where L_{tot} and L_{bulge} are the total and bulge luminosities, respectively (Lelli et al. 2016). The stellar mass of the bulge is given by $M_{\text{★bulge}}/M_{\odot} =$

⁷ Some rotation curves do not have a noticeable outer part. Thus, Chae et al. (2022) used only 114 galaxies.

⁸ Observed rotationally supported galaxies can be thinner or thicker than $h_z/R_d = 0.08$. However, the effect of varying h_z/R_d is minor unless the galaxy becomes close to the spherical shape (Chae & Milgrom 2022).

$0.7L_{\text{bulge}}/L_{\odot}$. The mass of the gas disk is given by $M_{\text{gas}} = 1.36M_{\text{HI}}$ where M_{HI} is the mass of neutral hydrogen (Lelli et al. 2016) and the factor 1.36 accounts for other gases, especially primordial helium (Chae et al. 2020; McGaugh et al. 2020).

According to the study by Chae & Milgrom (2022), the azimuthally averaged radial acceleration depends on the strength of the external field but has little dependence on its inclination. On the other hand, the radial acceleration in the inner part is essentially fixed by the disk geometry. A typical external field ($\tilde{e} \lesssim 0.1$) has a minor secondary effect both in AQUAL and QUMOND. It is thus sufficient to consider the axisymmetric case that the external field is aligned with the rotation axis in predicting the azimuthally averaged radial acceleration in rotation curves. We use the AQUAL numerical code (Chae & Milgrom 2022) developed recently based on the algorithm proposed by Milgrom (1986). Here the code is adjusted to include the multiple components of a galaxy, all of which are analytical. The code returns simulated ($g_{\text{bar}}, g_{\text{obs}}$) at the observed radii in each rotation curve of 152 SPARC galaxies. Note that azimuthal averaging is not required as the model is axisymmetric in the Chae & Milgrom (2022) code.

B. POSTERIOR PROPERTIES OF DARK MATTER HALOS

MCMC modeling has returned posterior probability density functions (PDFs) of all model parameters. Here posterior values of the halo parameters are compared with their prior values. Also, posterior values of the DM halo density slope between 1 and 2 per cent of r_{200} are compared with predictions from various cosmological hydrodynamic simulations.

B.1. $M_{\star} - M_{200}$ relation

The stellar mass (M_{\star}) – halo mass (M_{200}) relation is a major prior input in DM halo modeling. It is thus important to check whether posterior relations from MCMC results agree with the prior relation. Two prior $M_{\star} - M_{200}$ relations (that cover the range of currently available results in the literature) are used in MCMC modeling. Figure 7 shows the posterior relations from the MCMC results for three halo models. Because a scatter of 0.1 dex was allowed (for M_{\star} at fixed M_{200}) in MCMC modeling, the posterior values are scattered around the prior relation. When the prior from Kravtsov et al. (2018) is used (Figure 7(A)), the posterior results agree with the prior relation for all three models. Interestingly, even when the prior from Behroozi et al. (2013) is used (Figure 7(B)), the posterior results still better agree with the Kravtsov et al. (2018) relation rather than the Behroozi et al. (2013) relation. The SPARC galaxies prefer the Kravtsov et al. (2018) relation.

B.2. Halo concentration

When DM halos from DM only simulations are described by the NFW profile (the case of $(\alpha, \beta, \gamma) = (1, 3, 1)$ in Equation (4)) or the Einasto profile (the case of $r_c = 0$ in Equation (A15)), the scale radius r_s or \tilde{r}_s is the radius where the logarithmic slope is -2 . The concentration $c_{200}(= r_{200}/r_s)$ or $\tilde{c}_{200}(= r_{200}/\tilde{r}_s)$ is well predicted from DM only simulations under the Λ CDM cosmology. However, according to Λ CDM hydrodynamic simulations of galaxy formation, the baryonic physics of galaxy formation is expected to modify the halo mass distribution to a varying degree so that the profile is no longer NFW or Einasto in general. Consequently, in baryonic feedback affected halos the scale radius r_s or \tilde{r}_s no longer corresponds to the radius where the slope is -2 . For this reason, c_{200} or \tilde{c}_{200} is not constrained in MCMC modeling. However, an indirect constraint on c_{200} was presented from the DC14 simulations as a scaling relation for c_{-2}/c_{NFW} given by Equation (A13) where c_{-2} is the radius where the slope is -2 for the modified halo mass profile. This constraint was used only for the DC14 modeling.

Figure 8 shows the posterior values of c_{-2} derived from the MCMC modeling results for the three halo models. The upper panel shows the posterior relation of c_{-2} with M_{200} and compares it with the prediction from the Λ CDM DM only simulation (Dutton & Maccio 2014) under the Planck cosmology. The DC14 median is above the Λ CDM prediction for the whole range of M_{200} . The NIHAO and FIRE-2 medians are lower than the Λ CDM prediction for $M_{200} \lesssim 10^{11}M_{\odot}$ but higher for $M_{200} \gtrsim 10^{11}M_{\odot}$. The lower panel of Figure 8 shows the posterior behavior of c_{-2}/c_{NFW} and compares with the DC14 prediction. The DC14 MCMC posterior median agrees with or slightly exceeds the DC14 prediction, but the NIHAO and FIRE-2 posterior medians are lower than the DC14 prediction.

B.3. Density slope between $r = 0.01r_{200}$ and $0.02r_{200}$

Various hydrodynamic simulations of galaxy formation in the literature (Di Cintio et al. 2014a; Tollet et al. 2016; Lazar et al. 2020; Maccio et al. 2020) provide values of the logarithmic slope of the mass density of the baryon feedback affected halos. The values have large uncertainties though some generic pattern is seen in all simulations as shown in

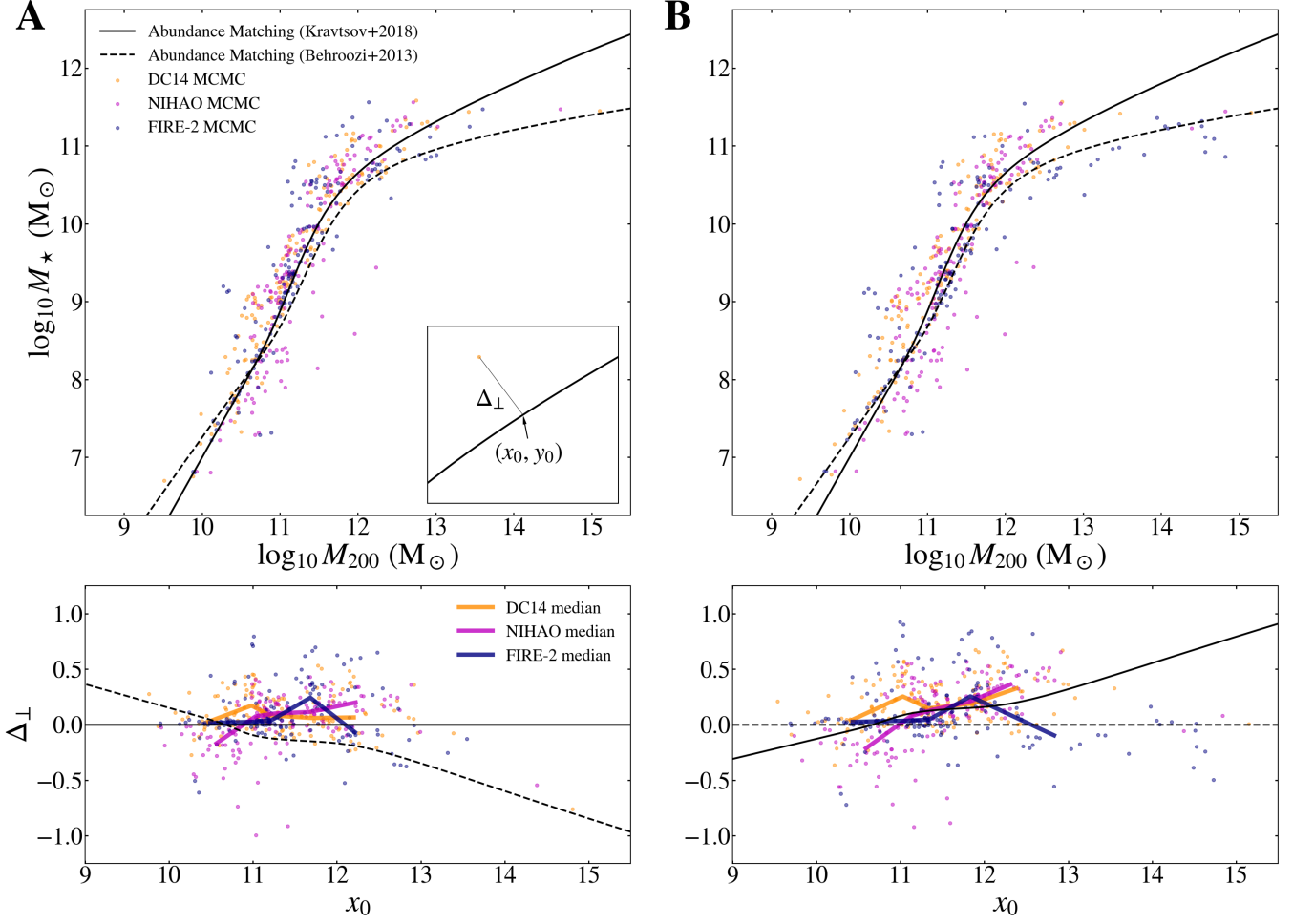


Figure 7. (A) Colored dots represent posterior values of stellar mass (M_*) and halo mass (M_{200}) from MCMC modeling results for three halo models. The prior relation between M_* and M_{200} is from the Kravtsov et al. (2018) abundance matching relation. Orthogonal residuals shown in the bottom panel indicate that the posterior median relations agree with the prior relation. (B) The MCMC results based on the prior relation between M_* and M_{200} from Behroozi et al. (2013). Even in this case, the posterior median relations agree better with the Kravtsov et al. (2018) abundance matching relation.

Fig. 9. Only for the NIHAO model was the predicted slope used as a prior for self-consistency. The more recent study by Maccio et al. (2020) considered both cases with and without black hole (BH) feedback, while the earlier studies (Di Cintio et al. 2014a; Tollet et al. 2016; Lazar et al. 2020) considered only the case without BH feedback. This can be important for massive galaxies with halo mass $M_{200} \gtrsim 4 \times 10^{12} M_\odot$, but the majority of SPARC galaxies are not so massive (see Figure 7). The likely range from the Maccio et al. (2020) case without BH feedback represented by the red band roughly includes all current results.

The DC14 MCMC results, although not constrained by any of the predicted slopes, reveal a well-defined relation between the slope and the ratio M_*/M_{200} . This relation is well within the red band from Maccio et al. (2020). Note also that the DC14 results are in better agreement with the SPARC data than the NIHAO and FIRE-2 results as shown in Figure 3. The NIHAO and FIRE-2 modeling results give a somewhat scattered distribution of the slope. The NIHAO modeling results match better with the blue band (the case with the BH feedback). The FIRE-2 results roughly match the Lazar et al. (2020) prediction based on the FIRE-2 simulations. This indicates self-consistency for the FIRE-2 results.

B.4. Scaling of three slope parameters of the DC14 model

The DC14 (Di Cintio et al. 2014b) simulations provide scaling relations of three indices α , β , and γ as given in Equation (A12). These relations were used as priors with a small scatter of 0.05 in producing MCMC results for the

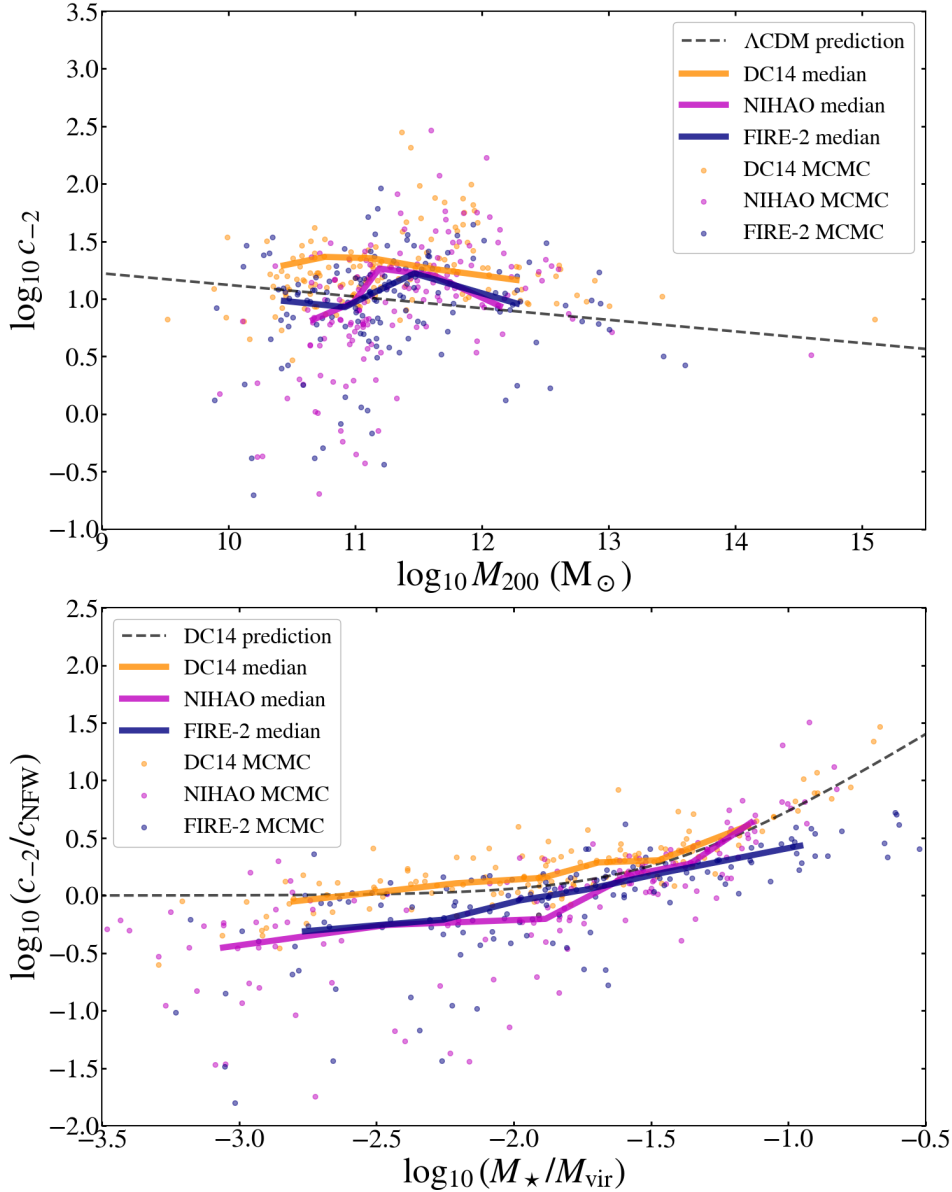


Figure 8. (Upper panel) Colored dots represent posterior values of $c_{-2} (\equiv r_{200}/r_{-2})$ where r_{-2} is the radius where the logarithmic slope of the halo density is -2 . The posterior values are compared with the NFW (Navarro et al. 1997) concentration from a Λ CDM dark matter only simulation assuming the Planck cosmology (Dutton & Maccio 2014). (Lower panel) The posterior values of the ratio c_{-2}/c_{NFW} (where c_{NFW} is the NFW concentration from the Λ CDM dark matter only simulation) are compared with the DC14 simulations prediction (Di Cintio et al. 2014b) represented by the dashed curve. Note that the prior relation was imposed only in obtaining the DC14 MCMC results.

DC14 model. Here we use Figure 10 to check whether the posterior results show any systematic deviation from the prior relations. Overall, the posterior results match adequately the prior relations. The inner slope γ does not show any sign of systematic deviation. The outer slope β tends to be a little higher than the prior value for $\log_{10}(M_{\star}/M_{200}) < -2$. The transition index α tends to be higher than the imposed minimum value of 0.5 for high values of $\log_{10}(M_{\star}/M_{200})$.

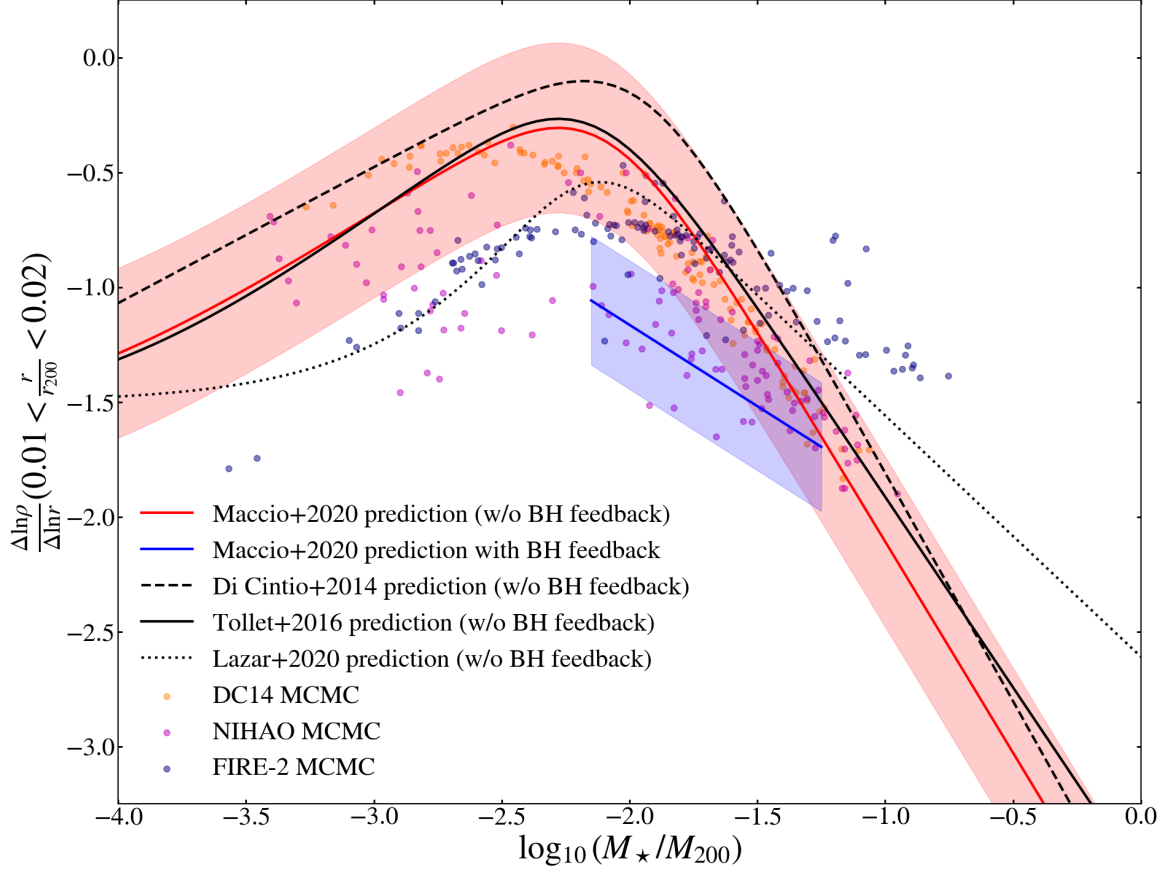


Figure 9. Posterior values of the logarithmic slope of the halo density between $r = 0.01r_{200}$ and $0.02r_{200}$ are compared with the prediction from various cosmological hydrodynamic simulations of galaxy formation. The red band represents the uncertainty from the Maccio et al. (2020) simulations without black hole (BH) feedback. This band roughly covers the range from all previous simulations without BH feedback. The blue band represents the uncertainty for halos with $M_{200} \gtrsim 4 \times 10^{12} M_{\odot}$ from the Maccio et al. (2020) simulations with BH feedback.

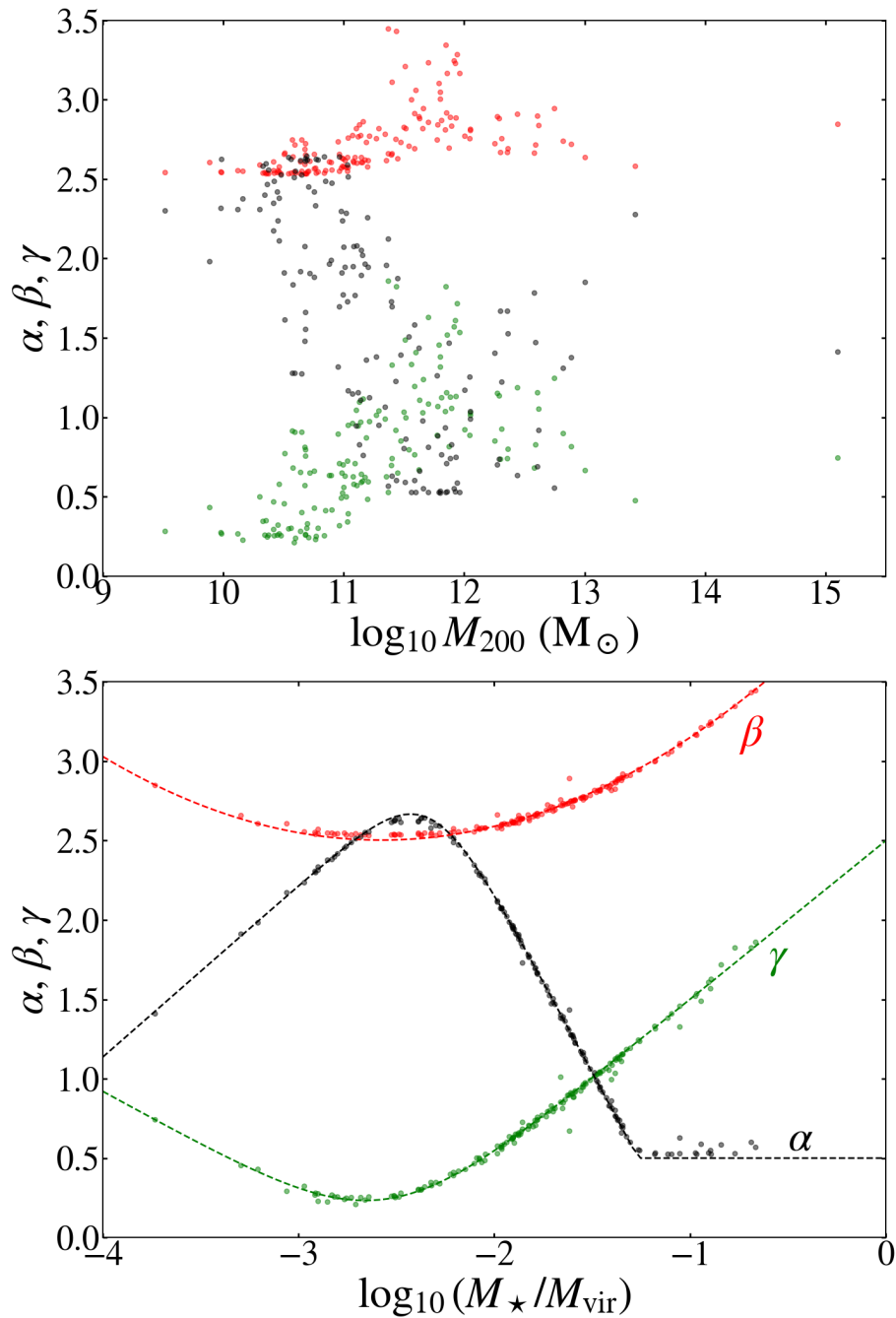


Figure 10. Colored dots represent posterior values of three indices of the halo model given by Equation (4) from the DC14 modeling results. The bottom panel compares the posterior values with the DC14 prior values (Di Cintio et al. 2014b) represented by dashed curves.